Low-Radiation Multiple-Coil Wireless Charger Using Detuned Compensation

Heyuan Li, *Graduate Student Member, IEEE*, Xiaoxuan Ji, *Graduate Student Member, IEEE*,
Xufeng Kou, *Member, IEEE*, Haoyu Wang, *Senior Member, IEEE*,
and Minfan Fu, *Senior Member, IEEE*

***Abstract*—This article investigates a low-radiation multicoil wireless charger driven by a single inverter, addressing the challenge of reducing radiation from unloaded transmitter (TX) coils in multicoil systems. Traditional methods often require multiple inverters or complex switching techniques to selectively activate TX coils, which increases system complexity and cost. Instead, this work proposes a detuned compensation technique that naturally attenuates the current in unloaded TX coils, thereby reducing radiation without the need for additional control circuits. The approach is analyzed using a two-coil system and then extended to a more general multicoil scenario. A five-coil TX system is experimentally demonstrated, achieving a current attenuation ratio exceeding 6 and maintaining an efficiency above 70% when charging a single 10-W receiver (RX). The results show a significant reduction in radiation field strength compared to a benchmark system, validating the effectiveness of the proposed detuned compensation technique. This method offers a promising solution for low-radiation wireless charging in applications requiring high mobility and adaptability.**

***Index Terms*—Current attenuation effect, detuned compensation, inductive power transfer (IPT), multicoil transmitter (TX).**

I. INTRODUCTION

INDUCTIVE power transfer (IPT) has experienced significant advancements and widespread adoption in charging applications [smartphone, electric vehicle (EV), etc.] [1], [2], [3]. The magnetic flux generated by the transmitter (TX) is efficiently coupled to the receiver (RX) through an isolated coupler [4], [5], [6]. To enhance steady-state performance, various compensation networks and active circuits such as inverters and rectifiers have been developed [7], [8], [9], [10], [11]. Multicoil techniques have been extensively discussed to meet the demands for greater mobility and adaptability to different charging devices [12], [13], [14], [15], [16], [17]. This makes multicoil technology highly attractive in the charging of smartphones, smartwatches, drones, and even moving EVs.

Previous studies have shown that independently driving each TX coil using its own inverter can allow for precise control of flux concentration in regions where the RXs are located [18], [19]. This approach, which involves modulating coil current or flux, enhances overall efficiency and minimizes radiation losses. However, as the number of TX coils increases, it introduces the challenge of efficiently driving these multiple coils. Additionally, this method requires the integration of extra sensing and control circuits to regulate and coordinate each coil's operation, ensuring system stability and optimal performance. To avoid the need for multiple inverters, an alternative driving technique involving a single inverter and a relay can be employed to selectively activate the TX coils. However, this method lacks the ability to modulate the magnetic field. The aforementioned approaches that involve switching-based techniques offer more promising solutions for high-power applications that prioritize efficiency.

In low-power scenarios, a straightforward circuit design with multiple functions is preferred. A typical approach is to connect multiple TX coils in series and drive them with a single inverter, effectively functioning as a single-TX single-RX system [20], [21], [22], [23]. However, this setup can lead to increased conduction losses and undesirable radiation, as even weakly coupled TX coils can become active. Recent studies, such as those in [20] and [21], explore solutions like using a multilevel switched-capacitor ac–dc rectifier for better efficiency and compactness, or a multichannel system for enhanced control and reduced interference. Nonetheless, radiation challenges persist. To tackle radiation issues, various strategies have been suggested. For example, Lee et al. [24] propose a hybrid loop array to optimize coil arrangement and minimize magnetic field interference. Additionally, Campi et al. [25] introduce active coils that dynamically cancel magnetic fields. Other studies, such as [26] and [27], have experimented with modifying coupler shapes and increasing coil numbers to improve coupling efficiency and stabilize the magnetic field. These efforts collectively aim to enhance wireless charging performance by effectively managing radiation problems.

This article presents a detuned compensation to mitigate radiation issues in multicoil systems. Unlike traditional methods that rely on multiple inverters or switches, the proposed

---

Received 22 November 2024; revised 25 February 2025 and 25 March 2025; accepted 18 April 2025. Date of publication 21 May 2025; date of current version 21 November 2025. This work was supported in part by the National Natural Science Foundation of China under Grant 52477013 and in part by Lingang Laboratory under Grant LG-GG-202402-06-10. *(Corresponding author: Minfan Fu.)*

Heyuan Li and Xiaoxuan Ji are with the School of Information Science and Technology, ShanghaiTech University, Shanghai 201210, China (e-mail: lihy4@shanghaitech.edu.cn; jixx@shanghaitech.edu.cn).

Xufeng Kou, Haoyu Wang, and Minfan Fu are with the School of Information Science and Technology, ShanghaiTech University, Shanghai 201210, China, and also with Shanghai Engineering Research Center of Energy Efficient and Custom AI IC, Shanghai 201210, China, (e-mail: kouxf@shanghaitech.edu.cn; wanghy@shanghaitech.edu.cn; fumf@shanghaitech.edu.cn).

Digital Object Identifier 10.1109/TIE.2025.3566720

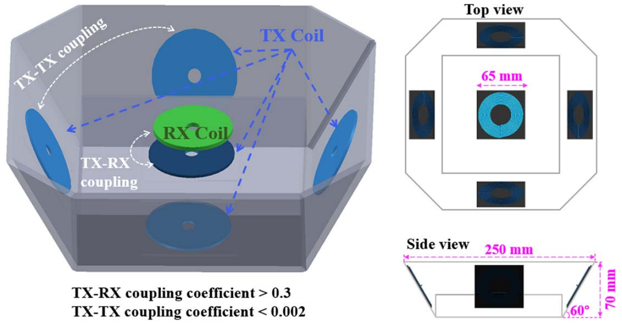

Fig. 1. Bowl-shape TX.

technique utilizes a detuned resonant tank to introduce reactive components. This load-dependent reactance enables a more natural response, resulting in improved radiation performance. To illustrate the effectiveness of the detuned compensation approach, a single-RX system with two TX coils is used as a case study. A circuit-model-based analysis is performed to assess the system efficiency and coil current. The current attenuation ratio is defined and optimized using detuning factors. Furthermore, the proposed detuned technique is generalized and applied to other basic compensations and TX systems with multiple coils. The advantages of the detuned system are demonstrated using a system with five TX coils. Overall, the detuned compensation technique offers a promising solution for reducing radiation issues in multicoil systems without the need for multiple inverters or switches. The results from the study provide insights into optimizing system performance and validating the efficacy of the proposed approach.

II. DETUNED RESONANT TANK

A. Practical Demand

To improve the flexibility of the RX, a widely used strategy involves employing a multicoil TX. As shown in Fig. 1, a bowl-shaped TX with four side coils and one central coil is presented as an example. Notably, all TX coils are designed to be identical, ensuring uniform performance. The bowl-shaped TX design serves two key purposes: it minimizes cross coupling between the TX coils and provides a stable position for the RX. The specific dimensions of the coils and the bowl are detailed in [9]. When an RX coil is placed on any part of the TX, the corresponding TX coil must be activated to fulfill the power requirements. The TX-RX coupling is strong enough for effective power transfer, with a coupling coefficient exceeding 0.3. Meanwhile, the coupling coefficient between adjacent TX coils is approximately 0.0017, and between TX coils along the same axis is about 0.0008. These low values of cross coupling ensure minimal interference between TX coils, further enhancing the efficiency of the multicoil design. This article investigates the fundamental principles of driving multiple TX coils without relying on complex switching techniques. The bowl-shaped TX is used as a representative example due to its compact design and minimal TX–TX cross coupling, but the proposed approach can be adapted to other TX structures with similarly limited cross coupling.

When the TX coils are connected in series, as depicted in Fig. 2(a), the RX benefits from the load perspective, as it can receive power at any position. However, a disadvantage of this configuration is that all the coils are activated, leading to unnecessary conduction losses and radiation issues, especially for the unloaded TX coils. In high-power applications such as dynamic charging of EVs, switching techniques are often employed to selectively activate the corresponding TX coil. This can be achieved by using multiple inverters or a single inverter with multiple relays. However, in low-power applications, there is sufficient design margin to strike a better balance between efficiency and cost performance.

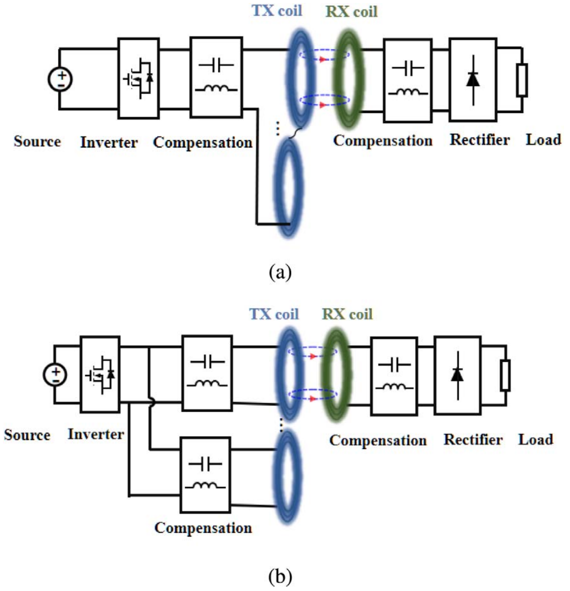

Fig. 2. Two basic driving schemes for multiple TX coils. (a) Using series TX coils (benchmark). (b) Using parallel TX compensation (proposed).

This article aims to investigate a system configuration depicted in Fig. 2(b), where the TX coils are not directly coupled to each other (i.e., not connected in series and parallel at their terminals). Each TX coil is individually compensated and connected in parallel to the inverter ac output. The objective is to utilize detuned techniques for TX/RX compensation, allowing for a natural response where the current of the loaded center TX coil is significantly higher than that of the unloaded side coils shown in Fig. 1. This behavior indicates that TX coils with weak coupling to the RX coil should be deactivated naturally, without the need for additional sensing, control, or activation circuits. By operating off-resonance, the detuned techniques tradeoff conduction loss to reduce radiation, eliminating the need for complex switching techniques.

B. Steady-State Model

This article aims to investigate the detuned characteristics of a resonant tank in a two-TX system using series-parallel (S-P) compensation. While the topology is widely used, most previous studies have centered on fine-tuned networks. This article aims to introduce a detuning technique to adjust the current distribution. The findings derived from this basic configuration will be generalized to apply to a broader range of multiple TX scenarios.

The modeling of the entire system aims to analyze the coil radiation at fundamental frequency and have the following

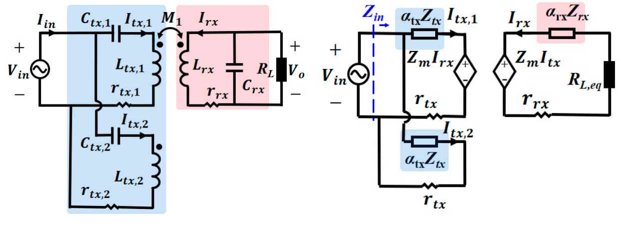

(a) (b)

Fig. 3. System using two TX coils. (a) Resonant tank. (b) Equivalent circuit model using detuning factors.

approximation. To accurately obtain fundamental current information, the fundamental approximation can be applied. In this context, the high-frequency parameters of the inverter and resonant tank do not affect the accuracy of the analysis. However, because the target system requires reactive power and has significant conduction losses, it is important to fully consider the impact of parasitic resistances. According to [28], the high-frequency rectifier model should consider the effects of junction capacitance. At the selected frequency of 1 MHz in this study, the input impedance of the rectifier is still dominated by its real part, allowing it to be modeled as a resistor.

Fig. 3 illustrates the system configuration, where $L_{\mathrm{tx},1}$ and $L_{\mathrm{tx},2}$ represent the inductance of the TX coils. Both TX coils are series compensated with capacitors $C_{\mathrm{tx},1}$ and $C_{\mathrm{tx},2}$, respectively. It is important to note that the TX coils and their respective compensations are identical. At the RX side, a parallel capacitor C_{rx} is introduced to compensate for the RX coil inductance L_{rx}. When the RX coil is placed directly above TX1, M_1 represents the mutual inductance between $L_{\mathrm{tx},1}$ and L_{rx}, with the coupling coefficient denoted as $k_1 = (M_1/\sqrt{L_{\mathrm{tx},1}L_{\mathrm{rx}}})$. It is worth mentioning that there is no coupling between $L_{\mathrm{tx},2}$ and L_{rx}, as the RX coil only couples with a single TX coil in this configuration.

In the resonant tank configuration shown in Fig. 3(a), the input voltage and current are denoted as v_{in} and i_{in}, respectively, while the output voltage is represented by v_{o}. The currents flowing through the two TX coils and the single RX coil are denoted as $i_{\mathrm{tx},1}$, $i_{\mathrm{tx},2}$, and i_{rx}. The equivalent ac load resistance is denoted as R_{L}, and r with different subscripts refers to the equivalent series resistances (ESRs) of the coils. Under the fundamental approximation, a phasor analysis is applied to the resonant tank, where all time-varying state variables are expressed in their phasor form. For example, $\boldsymbol{I}_{\mathrm{tx},1}$ represents the phasor form of $i_{\mathrm{tx},1}$, and $I_{\mathrm{tx},1}$ represents the magnitude of the corresponding current. In this context, a current attenuation factor, denoted as G, is introduced to evaluate the relationship between the main energy transfer coil and the other coil. It is defined as follows:

$$G = \frac{I_{\mathrm{tx},1}}{I_{\mathrm{tx},2}}. \tag{1}$$

The main objective is to design the compensations $C_{\mathrm{tx},1}$ (equivalent to $C_{\mathrm{tx},2}$) and C_{rx} in such a way that a high value of G is achieved.

On the TX side, the coil impedance $\boldsymbol{Z}_{\mathrm{tx}} = j\omega L_{\mathrm{tx},1}$ serves as a reference for normalization. For instance, the overall impedance of $L_{\mathrm{tx},1}$ and $C_{\mathrm{tx},1}$ is given by $j\omega L_{\mathrm{tx},1} + (1/j\omega C_{\mathrm{tx},1})$, which equals zero under perfect resonance. A detuning factor, denoted as α_{tx}, is introduced to evaluate the residual imaginary part after compensation. It is defined as

$$\alpha_{\mathrm{tx}} = \frac{\left(\omega L_{\mathrm{tx},1} - \frac{1}{\omega C_{\mathrm{tx},1}}\right)}{Z_{\mathrm{tx}}} = 1 - \frac{1}{\omega^2 L_{\mathrm{tx},1} C_{\mathrm{tx},1}} \tag{2}$$

where a zero value of α_{tx} indicates perfect resonance.

For the RX side, the RX coil inductance $\boldsymbol{Z}_{\mathrm{rx}} = j\omega L_{\mathrm{rx}}$ is used as the reference for normalization. Unlike the series compensation in the TX circuit, the parallel compensation in the RX circuit does not directly define the detuning factor [29]. Therefore, the parallel circuit consisting of C_{rx} and R_L is equivalently transformed into a series circuit, as shown in Fig. 3(b), according to the voltage source model. In this transformed model, the imaginary part of the RX circuit is represented by $\alpha_{\mathrm{rx}}\boldsymbol{Z}_{\mathrm{rx}}$, and the real part corresponds to the equivalent load $R_{L,\mathrm{eq}}$. Similar to α_{tx}, the relationship between the imaginary and real parts of the impedance can be derived as

$$\begin{cases} \alpha_{\mathrm{rx}} = 1 - \dfrac{C_{\mathrm{rx}} R_L^2}{L_{\mathrm{rx}}(1 + \omega^2 C_{\mathrm{rx}}^2 R_L^2)} \\ R_{L,\mathrm{eq}} = \dfrac{R_L}{1 + \omega^2 C_{\mathrm{rx}}^2 R_L^2} \end{cases} \tag{3}$$

where ω is the angular frequency. The impedance of the mutual inductance is denoted as $\boldsymbol{Z_m} = j\omega M$, and the two induced voltage sources are represented as $\boldsymbol{Z_m I_{\mathrm{rx}}}$ and $\boldsymbol{Z_m I_{\mathrm{tx},1}}$. $\boldsymbol{Z_{\mathrm{in}}}$ is the impedance seen by the inverter.

The circuit shown in Fig. 3(b) leads to the following set of Kirchhoff's voltage law (KVL) equations:

$$\begin{cases} (\alpha_{\mathrm{tx}}\boldsymbol{Z_{\mathrm{tx}}} + r_{\mathrm{tx}})\boldsymbol{I_{\mathrm{tx},1}} + \boldsymbol{Z_m I_{\mathrm{rx}}} = \boldsymbol{V}_{\mathrm{in}} \\ (\alpha_{\mathrm{tx}}\boldsymbol{Z_{\mathrm{tx}}} + r_{\mathrm{tx}})\boldsymbol{I_{\mathrm{tx},2}} = \boldsymbol{V}_{\mathrm{in}} \\ \boldsymbol{Z_m I_{\mathrm{tx},1}} + (\alpha_{\mathrm{rx}}\boldsymbol{Z_{\mathrm{rx}}} + r_{\mathrm{rx}} + R_{L,\mathrm{eq}})\boldsymbol{I_{\mathrm{rx}}} = 0. \end{cases} \tag{4}$$

Based on the previously mentioned formulas and calculations, the expressions for determining the coil currents can be deduced as follows:

$$\begin{cases} \boldsymbol{I_{\mathrm{tx},1}} = \dfrac{\alpha_{\mathrm{rx}}\boldsymbol{Z_{\mathrm{rx}}} + r_{\mathrm{rx}} + R_L}{-\boldsymbol{Z_m^2} + (\alpha_{\mathrm{tx}}\boldsymbol{Z_{\mathrm{tx}}} + r_{\mathrm{tx}})(\alpha_{\mathrm{rx}}\boldsymbol{Z_{\mathrm{rx}}} + r_{\mathrm{rx}} + R_L)} \boldsymbol{V_{\mathrm{in}}} \\ \boldsymbol{I_{\mathrm{tx},2}} = \dfrac{1}{r_{\mathrm{tx}} + \alpha_{\mathrm{tx}}\boldsymbol{Z_{\mathrm{tx}}}} \boldsymbol{V_{\mathrm{in}}} \\ \boldsymbol{I_{\mathrm{rx}}} = \dfrac{-\boldsymbol{Z_m}}{-\boldsymbol{Z_m^2} + (\alpha_{\mathrm{tx}}\boldsymbol{Z_{\mathrm{tx}}} + r_{\mathrm{tx}})(\alpha_{\mathrm{rx}}\boldsymbol{Z_{\mathrm{rx}}} + r_{\mathrm{rx}} + R_L)} \boldsymbol{V_{\mathrm{in}}}. \end{cases} \tag{5}$$

The overall efficiency of the resonant tank can be expressed as the ratio of the output power (P_o) to the input power (P_{in}). Mathematically, it is given by

$$\begin{cases} \eta = \dfrac{P_o}{P_{\mathrm{in}}} = \dfrac{I_{\mathrm{rx}}^2 R_L}{I_{\mathrm{rx}}^2 R_L + {I_{\mathrm{tx},1}}^2 r_{\mathrm{tx}} + {I_{\mathrm{tx},2}}^2 r_{\mathrm{tx}} + {I_{\mathrm{rx}}}^2 r_{\mathrm{rx}}} \\ \quad = \dfrac{-k^2 Q_{\mathrm{tx}} Q_{\mathrm{rx}}}{-k^2 Q_{\mathrm{tx}} Q_{\mathrm{rx}} - k^2 Q_{\mathrm{tx}} Q_L - {\alpha_2}^2 Q_{\mathrm{rx}} Q_L + \dfrac{r_{\mathrm{rx}}}{R_L} + \dfrac{R_L}{r_{\mathrm{tx}}} + 2} \\ Q_{\mathrm{tx}} = \dfrac{\omega L_{\mathrm{tx},1}}{r_{\mathrm{tx},1}}, Q_{\mathrm{rx}} = \dfrac{\omega L_{\mathrm{rx}}}{r_{\mathrm{rx}}}, Q_L = \dfrac{\omega L_{\mathrm{rx}}}{R_{L,\mathrm{eq}}}. \end{cases} \tag{6}$$

TABLE I
COUPLER PARAMETERS

Symbol	Value	Symbol	Value
L_{tx}	31 μH	L_{rx}	34 μH
r_{tx}	648 mΩ	r_{rx}	762 mΩ
M	12.5 μH	f_s	1 MHz

The efficiency also depends on α_{rx}, which is related to the RX ESR. Notably, the efficiency does not change with α_{tx}. In practical scenarios, where the ESR values are relatively small compared to the branch impedance, the ESRs (r_{tx} and r_{rx}) can be neglected. This simplification allows for the derivation of the input impedance of the two TX tanks

$$\begin{cases} \boldsymbol{Z}_{\textbf{in},1} = \dfrac{\boldsymbol{V}_{\textbf{in}}}{\boldsymbol{I}_{\textbf{tx},1}} = \dfrac{k^2 Q_L + j(\alpha_{\text{tx}} + \alpha_{\text{tx}}\alpha_{\text{rx}}^2 Q_L^2 - \alpha_{\text{rx}} k_1^2 Q_L^2)}{1+\alpha_{\text{rx}}^2 Q_L^2}\,\omega L_{\text{tx}} \\ \boldsymbol{Z}_{\textbf{in},2} = \dfrac{\boldsymbol{V}_{\textbf{in}}}{\boldsymbol{I}_{\textbf{tx},2}} = r_{\text{tx}} + \alpha_{\text{tx}}\boldsymbol{Z}_{\textbf{tx}}. \end{cases} \tag{7}$$

The input impedance $\boldsymbol{Z}_{\textbf{in}}$ can be obtained by taking the parallel combination of $\boldsymbol{Z}_{\textbf{in},1}$ and $\boldsymbol{Z}_{\textbf{in},2}$. From (5), the current attenuation factor can be derived as follows:

$$\begin{aligned} G &= \frac{I_{\text{tx},1}}{I_{\text{tx},2}} \\ &= 1 + \frac{1}{\sqrt{\left(-1+\dfrac{\alpha_{\text{tx}}\alpha_{\text{rx}}}{k_1^2}+\dfrac{1}{k_1^2 Q_{\text{tx}} Q_L}\right)^2 - \left(\dfrac{\alpha_{\text{tx}}}{k_1^2 Q_{\text{rx}}}+\dfrac{\alpha_{\text{tx}}}{k_1^2 Q_L}+\dfrac{\alpha_{\text{rx}}}{k_1^2 Q_{\text{tx}}}\right)^2}}. \end{aligned} \tag{8}$$

C. Design of Detuned Factors

The S-P compensations demonstrated in the article have two design variables, α_{tx} and α_{rx}, which play a crucial role in achieving the desired objectives. The main objectives include maximizing the current attenuation factor (G), improving the overall efficiency (η), and achieving an inductive input impedance ($\boldsymbol{Z}_{\textbf{in}}$) to ensure zero-voltage switching (ZVS) operation.

To validate the proposed compensation method, a practical coupler configuration depicted in Fig. 1 is fabricated and utilized in the experiment. The relevant coupler parameters are listed in Table I. Based on these parameter and the mentioned equations, simulations were conducted in advanced design system (ADS), and the results were obtained. Specifically, when the coupler is configured with one central coil and one side coil, the values of G, η, and $\boldsymbol{Z}_{\textbf{in}}$ can be calculated and evaluated based on different combinations of α_{tx} and α_{rx}.

During the evaluation process, several constraints were defined, including a minimum value of G greater than 5, a minimum efficiency (η) requirement of 80%, and a positive phase of $\boldsymbol{Z}_{\textbf{in}}$ for the specified range of R_L values between 25 and 200 Ω. In Fig. 4, the influence of α_{tx} and α_{rx} on G is depicted for $R_L = 200\ \Omega$. The color region represents the surviving points that satisfy the aforementioned constraints. The color intensity corresponds to the value of G, with brighter colors indicating higher values. Notably, there is a point that maximizes the current attenuation factor (G). When the two coils are connected in series, the value of G is equal to 1. This result confirms that the detuning factors α_{tx} and α_{rx} naturally select the loaded TX coil that is strongly coupled to the RX coil, while deactivating the unloaded TX coils.

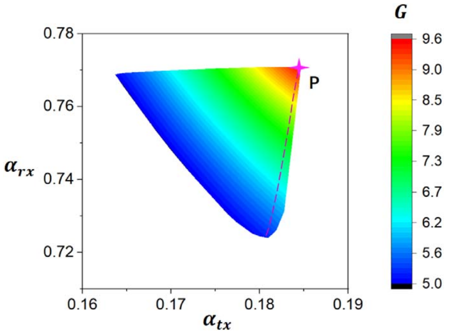

Fig. 4. Influence of α_{tx} and α_{rx} on G.

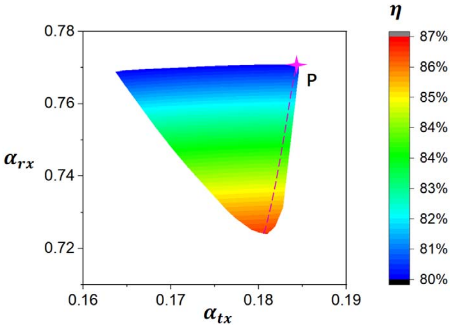

Fig. 5. Influence of α_{tx} and α_{rx} on η.

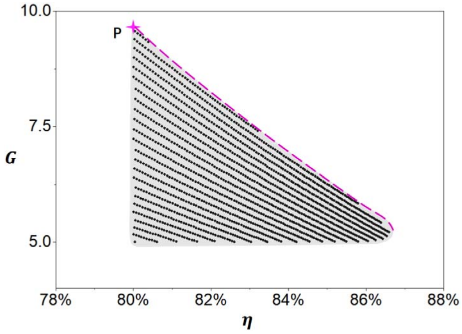

Fig. 6. Performance of G and η of all design points.

Similarly, an efficiency map can be plotted as shown in Fig. 5. From (6), it can be observed that the coupler efficiency is only affected by α_{rx} and is independent of α_{tx}. For convenience, the information from Figs. 4 and 5 can be merged into a single plot as shown in Fig. 6. The desired design point should lie on the pink line, which represents the tradeoff between G and η. In this case, point P is selected to maximize G. Fig. 7 demonstrates the performance of the coupler within the target load range of 20–200 Ω. It is important to note that during the selection of α_{tx} and α_{rx} candidates, a range of R_L values is already considered. Therefore, the resulting G and η values would not violate the given constraints of $G > 5$ and $\eta > 80\%$.

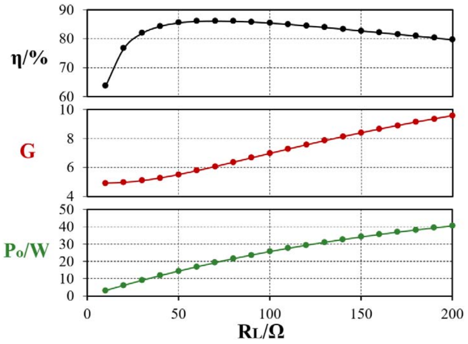

Fig. 7. G and η of point P under different load conditions.

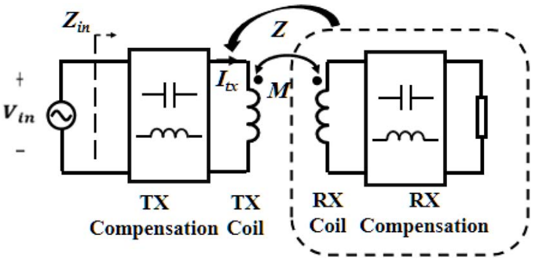

Fig. 8. Detuned mechanism.

III. EXTENSION OF DETUNED TECHNIQUES

A. Detuned Mechanism

Figs. 2(b) and 3 illustrate that the multiple TX tanks in a parallel configuration are effectively decoupled. Therefore, the current flowing through each TX coil is primarily influenced by the coupling condition. The phenomenon of current attenuation can be explained through a simplified one-TX one-RX scenario, as depicted in Fig. 8.

In the absence of an RX load, there is no reflected impedance at the TX coil. A detuned TX tank presents a high reactive impedance, resulting in a small current. When an RX coil is strongly coupled to the TX coil, a detuned RX introduces a reactive component that reflects back to the TX side, effectively reducing the net reactance of the TX tank. As a result, the TX coil is activated, and a current flows through it. In this detuned compensation approach, a detuned TX tank is used to attenuate the current in the absence of an RX load, while a detuned RX coil is employed to cancel out the large reactance introduced by the detuned TX coil. It is important to note that this effect cannot be achieved with perfect resonance conditions. However, this detuned system does result in higher conduction losses.

B. Comparison of Basic Compensations

The detuned compensation technique proposed in this article is applicable to various basic compensation configurations, including series–series (S-S), series–parallel (S-P), parallel–series (P-S), and parallel–parallel (P-P). These configurations all exhibit similar detuned effects. The simulated and calculated coupler values are based on the data in Table I. To ensure consistency, the parallel compensations are first transformed into a series circuit as shown in Fig. 9 and then normalized with respect to the coil impedance. This transformation has been applied to the RX side of the example S-P system.

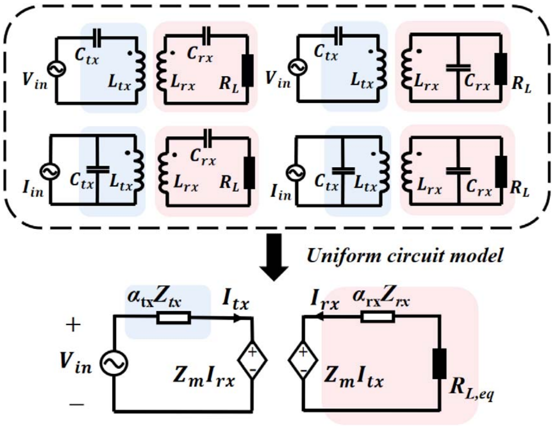

Fig. 9. Normalization model of detuning compensation network.

When parallel compensation is applied to the TX side, it is crucial to avoid using a clamped voltage source as the input excitation, as this would prevent the resonance effect of the shunt capacitors. Instead, a current source should be used. Despite this, the system can still be represented using a uniform equivalent circuit model, as shown in Fig. 9. The model parameters for all compensation configurations are derived and summarized in Table II for reference and comparison.

Similar to the detuning effect curve shown for the S-P compensation in the pink curve of Fig. 6, the other three compensations (S-S, P-P, and P-S) also offer similar benefits. However, since the voltage source is more commonly used, the tradeoff curve for S-S compensation is initially compared with the S-P compensation. Based on the parameters provided in Table I, if the load resistance R_L is within the range of [25, 200] Ω, there are no feasible design points for the S-S compensation. Alternatively, when R_L is in the range of [5, 10] Ω, a case design curve can be obtained as shown in Fig. 10. For this specific load range, the S-P compensation does not have any design points, indicating that the target detuning effect is dependent on the load range. Therefore, there is no universal conclusion for selecting the compensation technique.

Furthermore, in Fig. 10, the P-P and P-S compensations are also used to design a detuned system, but the suitable load ranges differ significantly. In this article, the S-P compensation is still utilized for further discussion and analysis.

C. Influence of TX-Coil Numbers

The conclusion drawn from the two-coil case can be directly extended to the N-coil case due to the parallel connection of the TX tanks. Assume that the RX coil is placed on the ith TX coil, and its current is the same as $I_{\mathrm{tx},1}$ given by (5)

$$I_{\mathrm{tx},i} = \frac{\alpha_2 Z_{\mathrm{rx}} + r_{\mathrm{rx}} + R_L}{-Z_m^2 + (\alpha_1 Z_{\mathrm{tx}} + r_{\mathrm{tx}})(\alpha_2 Z_{\mathrm{rx}} + r_{\mathrm{rx}} + R_L)}. \tag{9}$$

For the rest of the coils, their current is equal to $I_{\mathrm{tx},2}$ [as given by (5)]. Therefore, the current attenuation factor can be defined as the ratio between $I_{\mathrm{tx},i}$ and the average current of the

TABLE II
NORMALIZED MODEL PARAMETERS OF FOUR BASIC COMPENSATION NETWORKS

Compensation	V_{in}	α_{tx}	α_{rx}	$R_{L,\text{eq}}$
S-S	V_{in}	$1-\frac{1}{\omega^2 L_{\text{tx}} C_{\text{tx}}}$	$1-\frac{1}{\omega^2 L_{\text{rx}} C_{\text{rx}}}$	R_L
S-P	V_{in}	$1-\frac{1}{\omega^2 L_{\text{tx}} C_{\text{tx}}}$	$1-\frac{C_{\text{rx}} {R_L}^2}{L_{\text{rx}}(1+\omega^2 {C_{\text{rx}}}^2 {R_L}^2)}$	$\frac{R_L}{1+\omega^2 {C_{\text{rx}}}^2 {R_L}^2}$
P-S	$\frac{I_{\text{in}}}{j\omega C_{\text{tx}}}$	$1-\frac{1}{\omega^2 L_{\text{tx}} C_{\text{tx}}}$	$1-\frac{1}{\omega^2 L_{\text{rx}} C_{\text{rx}}}$	R_L
P-P	$\frac{I_{\text{in}}}{j\omega C_{\text{tx}}}$	$1-\frac{1}{\omega^2 L_{\text{tx}} C_{\text{tx}}}$	$1-\frac{C_{\text{rx}} {R_L}^2}{L_{\text{rx}}(1+\omega^2 {C_{\text{rx}}}^2 {R_L}^2)}$	$\frac{R_L}{1+\omega^2 {C_{\text{rx}}}^2 {R_L}^2}$

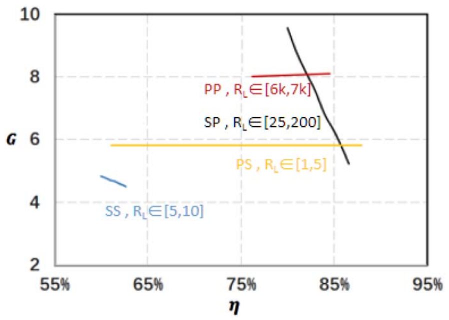

Fig. 10. Comparison of different compensations at different load ranges.

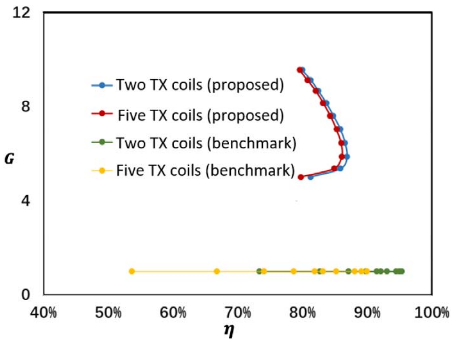

Fig. 11. Influence of coil number.

remaining TX coils, which is the same as (8). The efficiency of the resonant tank is then updated as

$$\eta = \frac{P_o}{P_{\text{in}}} = \frac{{I_{\text{rx}}}^2 R_L}{{I_{\text{rx}}}^2 R_L + {I_{\text{rx}}}^2 r_{\text{rx}} + \sum_{i=1}^{n} {I_{\text{tx},i}}^2 r_{\text{tx}}}. \tag{10}$$

Equation (10) shows that the efficiency will decrease with an increase in the number of coils.

In the case of the S-P compensation example, this article evaluates its performance by sweeping the load resistance, as shown in Fig. 11. The blue line in Fig. 11 represents the performance of the selected design point P in Fig. 10, and it contains the same information as Fig. 7. To compare the performance of the detuned system with a system without detuned techniques, it considers the scenario where two TX coils are connected in series, as depicted in Fig. 2. This configuration serves as a benchmark with no current attenuation effect, and thus the current attenuation factor (G) is equal to 1. The efficiency varies with changes in the load resistance, resulting in a straight green line in Fig. 11. In most cases, the benchmark system achieves higher efficiency. However, as the number of TX coils increases, the benchmark system experiences a rapid drop in efficiency, while the proposed detuned system maintains similar performance regardless of the number of coils. This indicates that the detuned system is more suitable for multicoil cases.

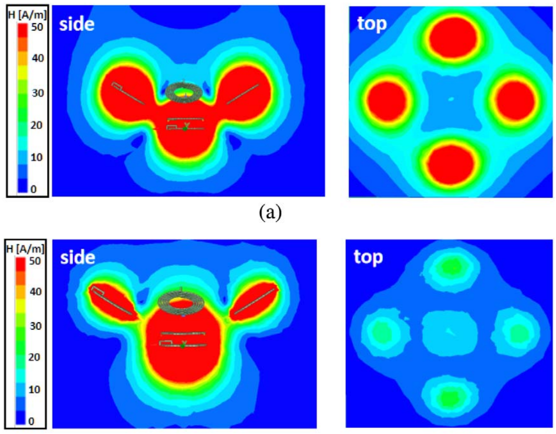

(a)

(b)

Fig. 12. Magnetic field distribution comparison. (a) Benchmark system. (b) Detuned system.

D. Magnetic Field Attenuation

To compare the magnetic field distribution between the proposed detuned system and the benchmark system, a simulation is performed under the same output power condition. In the simulation, the coupler shown in Fig. 1 with $N = 5$ coils is used, and only one RX coil is placed in the center region.

Fig. 12(a) illustrates the magnetic field distribution of the benchmark system, where each TX coil carries the same current. Both the top view and side view show the high radiation of the benchmark system. The bottom-loaded coil is activated for power transfer, and the side unloaded coils are also activated with the same current, which leads to unnecessary radiation. In contrast, Fig. 12(b) shows the magnetic field distribution for the detuned system. Due to the high current attenuation effect achieved by the detuning techniques, the current-induced magnetic fields are dramatically reduced, resulting in a significant

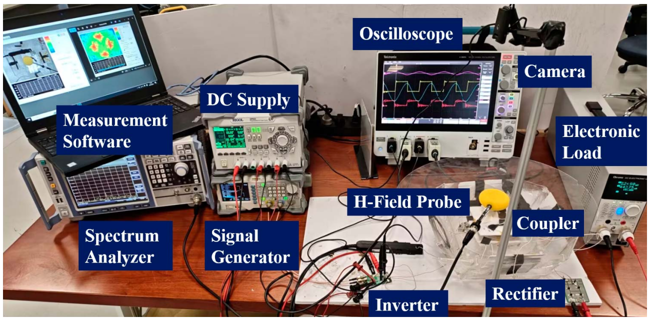

Fig. 13. Test setup for a bowl-shape TX.

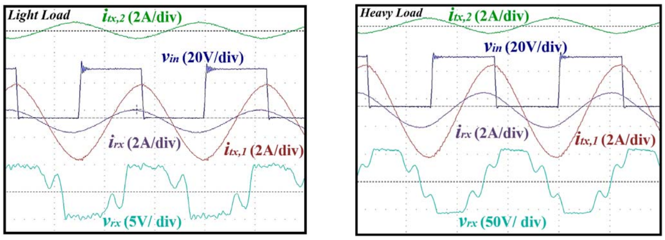

(a) (b)

Fig. 14. Typical waveform of a detuned system. (a) Light load condition. (b) Heavy load condition.

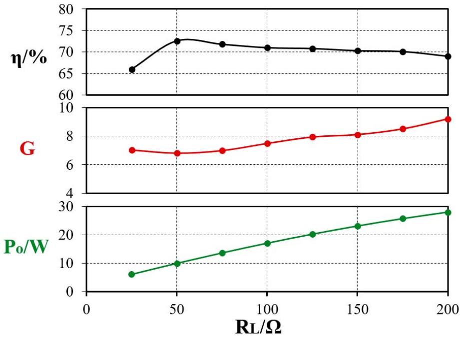

Fig. 15. Measured G and η under different load conditions.

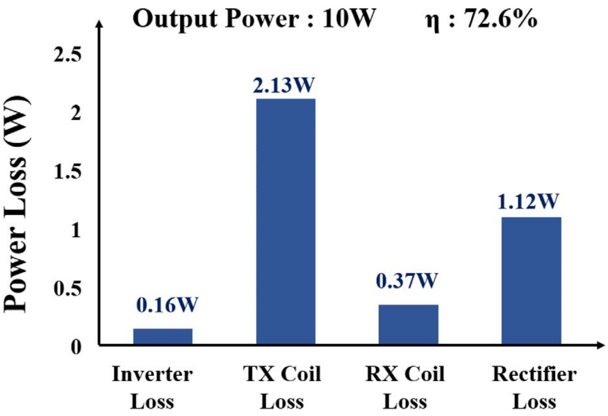

Fig. 16. Power loss distribution at peak efficiency point.

reduction in overall magnetic field radiation. Additionally, the system ensures power transfer capability by enhancing the magnetic field of the corresponding TX coil when the RX position changes or when multiple RX devices are present. For the multiple RX condition, the TX coils, without detuning, produce similar magnetic fields due to the consistent current distribution. This design allows for efficient power transfer to multiple devices while maintaining magnetic field homogeneity.

IV. EXPERIMENT VERIFICATION

As shown in the setup of Fig. 13, a prototype of a bowl-shaped charger was constructed according to Fig. 1. The system is driven by a half-bridge inverter with a constant dc input voltage of 20 V and tested under different load conditions. The TX series compensation capacitor and the RX parallel capacitor are 1 and 3 nF, respectively, both of which are NP0 standard ceramic capacitors. Using the same bowl-shape TX, two types of systems are built according to the configuration of Fig. 2 when using S-P compensation. The detailed coupler parameters are the same as the simulation in Table I. Additionally, a relevant field testing system was used for measurements. The compensation capacitors are chosen according to the design point P on the tradeoff curve in Fig. 4, where $\alpha_{\text{tx}} = 0.185$ and $\alpha_{\text{rx}} = 0.771$. The charger operates at a frequency of 1 MHz, driven by a half-bridge inverter. A bridge rectifier and an electronic load are employed on the RX side. The cross-coupling coefficient between the TX coils is less than 0.002.

The terminal waveforms of the system using the proposed detuned design are recorded and displayed in Fig. 14. The smooth voltage waveform (v_{in}) indicates that the inductive input impedance ($\boldsymbol{Z}_{\textbf{in}}$) assists in achieving ZVS in both light and heavy load conditions. At the RX side, the rectifier terminal voltage v_{rx} is also measured, and the voltage distortion is mainly due to the junction capacitance. The current waveform of $i_{\text{tx},1}$ is significantly larger than that of $i_{\text{tx},2}$, demonstrating the achievement of a high current attenuation factor (G). Overall, the recorded waveforms validate the effectiveness of the proposed detuned design in achieving the desired objectives.

As shown in Fig. 15, the overall efficiency and gain G of the system with the proposed detuning design were measured under various load conditions, with the corresponding power levels also provided. The results are consistent with the simulation results shown in Fig. 7. It is worth noting that the overall system efficiency is lower than the tank efficiency in the simulation results. This can be attributed to the additional losses introduced by the inverters and rectifiers in the overall system. The loss breakdown of the proposed system is shown in Fig. 16, and the RX coil and rectifier would still dominate the loss from the system perspective.

A benchmark system is also constructed to compare with the detuned system. The comparison is shown in Fig. 17, where both systems exhibit similar peak efficiencies. However, the detuned system demonstrates superior current attenuation capability. This experiment result is consistent with the simulation of Fig. 11.

The space-magnetic field visualization system (EPS-02Ev3, NoiseKen Inc.) can effectively measure the field distribution as shown in Fig. 18. With the help of a spectrum analyzer (FSV7, Rohde&Schwarz Inc.), the probe is able to detect the field magnitude for any position above the bowl [refer to Fig. 13]. Meanwhile, the camera is able to detect the position of the colored

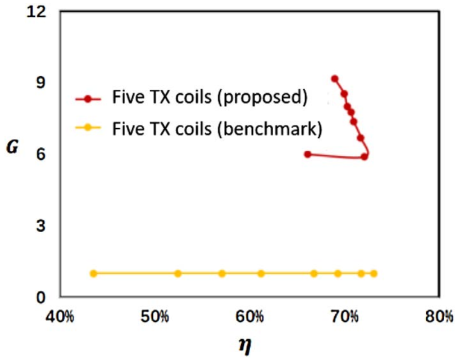

Fig. 17. G-η comparison between the detuned system and the benchmark one.

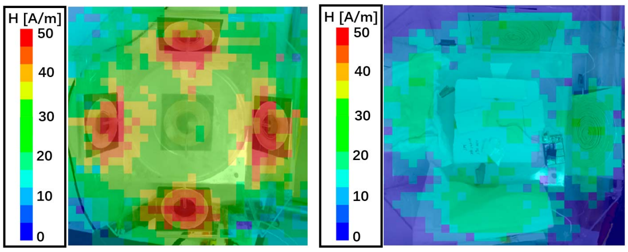

(a) (b)

Fig. 18. Measured field distribution comparison. (a) Benchmark system. (b) Detuned system.

TABLE III
COMPARISON BETWEEN THE PROPOSED METHOD AND OTHER RADIATION SUPPRESSION METHODS

Ref.	Output Power	Efficiency	Add. Comp.	Add. Cont.
[25]	7.7 kW	90.9%	Yes	Yes
[30]	50 kW	95.2%	No	Yes
[31]	1.09 kW	90%	Yes	No
[32]	200 W	80%	No	Yes
[24]	/	70.65%	Yes	No
[26]	380 W	87.5%	Yes	No
[27]	125 W	80.2%	Yes	No
[33]	60 W	91%	Yes	No
This work	10 W	72.6%	No	No

probe. Finally, all these field and position information will be synchronized through the laptop to give a visualized field distribution. The experimental results are consistent with the simulation results in Fig. 12, confirming the effectiveness of the detuned design in reducing magnetic field radiation.

A detailed comparison is provided in Table III. For applications that require a high level of power, efficiency takes precedence, making it beneficial to incorporate more passive components such as coils or shielding to diminish radiation. Concurrently, additional control is essential to adequately disable those TX coils associated with weak TX–RX coupling. As the power level falls, the appeal of using fewer additional components (comp.) or control (cont.) grows. The suggested methodology does not necessitate any extra comp. and cont. to effectively disable weakly coupled TX–RX channels. The proposed approach attempts to strike an attractive balance between radiation, efficiency, complexity, and cost.

V. CONCLUSION

This article proposes a detuned compensation technique to address the issue of radiation in unloaded coils in a multiple-coil system. The concept of current attenuation is introduced to quantify the degree of radiation reduction achieved by the detuned design. The analysis of the circuit model reveals the impact of the system detuned factors on both efficiency and current attenuation effect. The detuned design effectively utilizes the reactance resulting from the detuning to selectively activate the loaded TX coil, thereby reducing radiation. The current attenuation effects observed in this study can be easily extended to other compensation techniques and systems with a greater number of TX coils. The final prototype of the bowl-shaped charger demonstrates a current attenuation factor exceeding 6 and achieves a peak efficiency of 72.6% when charging a 10-W RX. The method proposed in this article is better suited for low to medium power applications. It naturally suppresses radiation by introducing reactive power, making it ideal for systems where simplicity is a priority over maximum efficiency.

REFERENCES

[1] J.-Q. Zhu, Y.-L. Ban, Y. Zhang, Z. Yan, R.-M. Xu, and C. C. Mi, "Three-coil wireless charging system for metal-cover smartphone applications," *IEEE Trans. Power Electron.*, vol. 35, no. 5, pp. 4847–4858, May 2020.

[2] X. Wang, R. He, H. Wang, J. Liang, and M. Fu, "Modified LCC compensation and magnetic integration for inductive power transfer," *IEEE J. Emerg. Sel. Topics Power Electron.*, vol. 12, no. 1, pp. 186–194, Feb. 2024.

[3] G. Ning, K. Zhou, J. Liang, H. Wang, and M. Fu, "Reconfigurable and modular wireless charger based on dual-band design," *IEEE Trans. Circuits Syst. II, Analog Digit. Signal Process.*, vol. 70, no. 9, pp. 3524–3528, Sep. 2023.

[4] F. Lu et al., "A tightly coupled inductive power transfer system for low-voltage and high-current charging of automatic guided vehicles," *IEEE Trans. Ind. Electron.*, vol. 66, no. 9, pp. 6867–6875, Sep. 2019.

[5] J. Lu, G. Zhu, D. Lin, S.-C. Wong, and J. Jiang, "Load-independent voltage and current transfer characteristics of high-order resonant network in IPT system," *IEEE J. Emerg. Sel. Topics Power Electron.*, vol. 7, no. 1, pp. 422–436, Mar. 2019.

[6] R. He, P. Zhao, M. Fu, Y. Liu, H. Wang, and J. Liang, "Decomposition and synthesis of high-order compensated inductive power transfer systems for improved output controllability," *IEEE Trans. Microw. Theory Techn.*, vol. 67, no. 11, pp. 4514–4523, Nov. 2019.

[7] Y. Zhang, S. Chen, X. Li, and Y. Tang, "Dual-side phase-shift control of wireless power transfer implemented on primary side based on driving windings," *IEEE Trans. Ind. Electron.*, vol. 68, no. 9, pp. 8999–9002, Sep. 2021.

[8] Z. Zhu et al., "Efficiency optimization and power allocation of omnidirectional wireless power transfer for multiple receivers," *IEEE Trans. Ind. Electron.*, vol. 70, no. 10, pp. 9689–9699, Oct. 2023.

[9] P. Zhao, X. Ji, H. Wang, and M. Fu, "H5-bridge-based bowl-shape wireless charger for multiple loads," *IEEE Trans. Ind. Electron.*, vol. 70, no. 9, pp. 8853–8861, Sep. 2023.

[10] K. Zhao, G. Ning, R. He, H. Yang, H. Wang, and M. Fu, "An unsymmetrical driving scheme for inductive power transfer systems using decoupled transmitter coils," *IEEE J. Emerg. Sel. Topics Ind. Electron.*, vol. 4, no. 2, pp. 614–624, Apr. 2023.

[11] S. Wang, Y. Yin, R. He, J. Liang, and M. Fu, "High-order compensated capacitive power transfer systems with misalignment insensitive resonance," *IEEE Trans. Circuits Syst. I, Fundam. Theory Appl.*, vol. 69, no. 8, pp. 3450–3460, Aug. 2022.

[12] X. Ji, P. Zhao, H. Wang, H. Yang, and M. Fu, "Multiple-receiver inductive power transfer system based on multiple-coil power relay module," *IEEE Trans. Circuits Syst. I, Fundam. Theory Appl.*, vol. 70, no. 6, pp. 2625–2634, Jun. 2023.

[13] G. Wei, J. Feng, J. Zhang, C. Wang, C. Zhu, and S. Yurievich Ostanin, "An efficient power and data synchronous transfer method for wireless

power transfer system using double-d coupling coil," *IEEE Trans. Ind. Electron.*, vol. 68, no. 11, pp. 10643–10653, Nov. 2021.

[14] S. Huh et al., "Transmitter coils selection method for wireless power transfer system with multiple transmitter coils and single receiver coil," *IEEE Trans. Power Electron.*, vol. 38, no. 3, pp. 4092–4109, Mar. 2023.

[15] R. He, X. Wang, H. Wang, and M. Fu, "Optimal terminals of a multitransmitter multireceiver inductive coupler with equality power constraints," *IEEE Trans. Power Electron.*, vol. 38, no. 10, pp. 11953–11963, Oct. 2023.

[16] L. Qian, K. Cui, H. Xia, H. Shao, J. Wang, and Y. Xia, "An inductive power transfer system for powering wireless sensor nodes in structural health monitoring applications," *IEEE Trans. Microw. Theory Techn.*, vol. 70, no. 7, pp. 3732–3740, Jul. 2022.

[17] D. Brizi, J. P. Stang, A. Monorchio, and G. Lazzi, "On the design of planar arrays of nonresonant coils for tunable wireless power transfer applications," *IEEE Trans. Microw. Theory Techn.*, vol. 68, no. 9, pp. 3814–3822, Sep. 2020.

[18] S. Liu et al., "An output power fluctuation suppression method of DWPT systems based on dual-receiver coils and voltage doubler rectifier," *IEEE Trans. Ind. Electron.*, vol. 70, no. 10, pp. 10167–10179, Oct. 2023.

[19] H. R. Rahnamaee, D. J. Thrimawithana, and U. K. Madawala, "Mosfet based multilevel converter for IPT systems," in *Proc. IEEE Int. Conf. Ind. Technol. (ICIT),* 2014, pp. 295–300.

[20] S. Cochran, C. Zhao, and D. Costinett, "Multilevel switched-capacitor AC–DC step-down rectifier for wireless charging with reduced conduction loss and harmonic content," *IEEE Trans. Power Electron.*, vol. 37, no. 7, pp. 8669–8681, Jul. 2022.

[21] Y. Huang, C. Liu, Y. Xiao, and S. Liu, "Separate power allocation and control method based on multiple power channels for wireless power transfer," *IEEE Trans. Power Electron.*, vol. 35, no. 9, pp. 9046–9056, Sep. 2020.

[22] A. Pacini, A. Costanzo, S. Aldhaher, and P. D. Mitcheson, "Load- and position-independent moving MHz WPT system based on GaN-distributed current sources," *IEEE Trans. Microw. Theory Techn.*, vol. 65, no. 12, pp. 5367–5376, Dec. 2017.

[23] J. Kim, D.-H. Kim, J. Choi, K.-H. Kim, and Y.-J. Park, "Free-positioning wireless charging system for small electronic devices using a bowl-shaped transmitting coil," *IEEE Trans. Microw. Theory Techn.*, vol. 63, no. 3, pp. 791–800, Mar. 2015.

[24] S. Lee et al., "Low leakage electromagnetic field level and high efficiency using a novel hybrid loop-array design for wireless high power transfer system," *IEEE Trans. Ind. Electron.*, vol. 66, no. 6, pp. 4356–4367, Jun. 2019.

[25] T. Campi, S. Cruciani, F. Maradei, and M. Feliziani, "Magnetic field mitigation by multicoil active shielding in electric vehicles equipped with wireless power charging system," *IEEE Trans. Electromagn. Compat.*, vol. 62, no. 4, pp. 1398–1405, Aug. 2020.

[26] W. Huang, Y. Zhang, F. Gao, and Y. Yang, "Magnetic structure design of wireless power transfer for free-rotating UAV with low stray magnetic fields," *IEEE Trans. Ind. Electron.*, vol. 72, no. 1, pp. 481–491, Jan. 2025.

[27] Y. Li, K. Xie, and Y. Ying, "A novel magnetic coupler with low leakage emf for auv wireless power transfer system," *IEEE J. Emerg. Sel. Topics Ind. Electron.*, vol. 5, no. 1, pp. 212–224, Jan. 2024.

[28] M. Fu, Z. Tang, and C. Ma, "Analysis and optimized design of compensation capacitors for a megahertz WPT system using full-bridge rectifier," *IEEE Trans. Ind. Informat.*, vol. 15, no. 1, pp. 95–104, Jan. 2019.

[29] P. Zhao, J. Liang, H. Wang, and M. Fu, "Detuned LCC/s-s compensation for stable-output inductive power transfer system under ultrawide coupling variation," *IEEE Trans. Power Electron.*, vol. 38, no. 10, pp. 12342–12347, 2023.

[30] A. U. Ibrahim, W. Zhong, and M. D. Xu, "A 50-kw three-channel wireless power transfer system with low stray magnetic field," *IEEE Trans. Power Electron.*, vol. 36, no. 9, pp. 9941–9954, Sep. 2021.

[31] P. Deng, C. Tang, M. Sun, Z. Liu, H. Hu, and T. Lin, "Emi suppression method for lcc-s mc-wpt systems by parameter optimization," *IEEE Trans. Power Electron.*, vol. 39, no. 9, pp. 11134–11147, Sep. 2024.

[32] S. A. Chowdhury, S.-W. Kim, S.-M. Kim, J. Moon, I.-K. Cho, and D. Ahn, "Automatic tuning receiver for improved efficiency and emi suppression in spread-spectrum wireless power transfer," *IEEE Trans. Ind. Electron.*, vol. 70, no. 1, pp. 352–363, Jan. 2023.

[33] Y. Li, K. Xie, Y. Ying, and Z. Li, "An improved hybrid shielding with lc coil for wireless power transfer system," *IEEE Trans. Electromagn. Compat.*, vol. 64, no. 3, pp. 720–731, Jun. 2022.

Heyuan Li (Graduate Student Member, IEEE) received the B.S. degree in electrical engineering from the University of Shanghai for Science and Technology, Shanghai, China, in 2020. He is currently working toward the Ph.D. degree in power electronics with the School of Information Science and Technology, ShanghaiTech University, Shanghai.

His current interests include radiation modeling and electromagnetic interference (EMI) of high-frequency power converters.

Xiaoxuan Ji (Graduate Student Member, IEEE) received the B.S. degree in automation from the Central South University, Changsha, China, in 2021, and the M.S. degree in circuit and systems from ShanghaiTech University, Shanghai, China.

Her research interest includes biomedical wireless power transfer.

Xufeng Kou (Member, IEEE) received the B.S. (Hons.) degree in optical engineering from Chu Kochen Honors College and Optical Engineering, Zhejiang University, Hangzhou, China, in 2009, and the M.S. and Ph.D. degrees in electrical engineering in 2012 and 2015, respectively, from the University of California Los Angeles (UCLA), Los Angeles, CA, USA, where he is currently working toward the Ph.D. degree with Prof. Kang L. Wang's group, focused on (magnetic) topological insulators, quantum anomalous Hall effect, and related spin-orbit coupling-enabled spintronic devices.

Currently, he is a Full Professor with tenure with the School of Information Science and Technology, Shanghai Technological University, Shanghai, China.

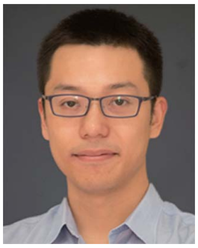

Haoyu Wang (Senior Member, IEEE) received the bachelor's(Hons.) degree from Zhejiang University, Hangzhou, China, in 2009, and the Ph.D. degree from the University of Maryland at College Park, College Park, MD, USA, in 2014, both in electrical engineering.

In 2014, he joined the School of Information Science and Technology, ShanghaiTech University, Shanghai, China, where he is currently a Full Professor with tenure. His research interests include power electronics, electric vehicles, renewable energy systems, and power management integrated circuits.

Dr. Wang is an Associate Editor of IEEE TRANSACTIONS ON INDUSTRIAL ELECTRONICS, IEEE TRANSACTIONS ON TRANSPORTATION ELECTRIFICATION, and *CPSS Transactions on Power Electronics and Applications*. He is a Guest Editor of IEEE JOURNAL OF EMERGING AND SELECTED TOPICS IN POWER ELECTRONICS and a Guest Associate Editor of IEEE TRANSACTIONS ON POWER ELECTRONICS.

Minfan Fu (Senior Member, IEEE) received the B.S., M.S., and Ph.D. degrees in electrical and computer engineering from the University of MichiganShanghai Jiao Tong University Joint Institute, Shanghai Jiao Tong University, Shanghai, China, in 2010, 2013, and 2016, respectively.

Currently, he is an Associate Professor with the School of Information Science and Technology, ShanghaiTech University, Shanghai. From 2016 to 2018, he held a postdoctoral researcher position with the Center for Power Electronics Systems (CPES), Virginia Polytechnic Institute and State University, Blacksburg, VA, USA. His research interests include megahertz wireless power transfer, high-frequency power conversion, high-frequency magnetic design, and the application of widebandgap devices. He holds one U.S. patent and seven Chinese patents, and has authored or co-authored more than 130 papers in prestigious IEEE journals and conferences.